

Phonon-assisted tunneling in an isolated double dot system

J. Martorell^a, D.W.L. Sprung^b, GuoHong Yun^{b,c}

*Departament d'Estructura i Constituents de la Materia, Facultat Física, University of Barcelona
Barcelona 08028, Spain*

^b*Department of Physics and Astronomy, McMaster University, Hamilton ON L8S 4M1 Canada*

^c*Department of Physics, Inner Mongolia University, Hohhot, 010021, P.R. China*

(November 7, 2018)

Phonon-assisted tunneling rates are evaluated for a well isolated double dot system defined in a GaAs semiconductor heterostructure of finite thickness. A separable model for the confining potential allows accurate determinations of doublet electron wavefunctions and energies. It is found that at small doublet energies the piezoelectric rates due to flexural modes give the dominant contribution. For small slab thicknesses the predicted rates are up to two orders of magnitude larger than for very thick slabs.

73.63.Kv,73.50.Rb,73.21.La

I. INTRODUCTION

The problem we consider is the transfer of an electron between two dots separated by a tunneling barrier. The experimental situation we have in mind is that of two contiguous dots defined by electrostatic confinement, as in the experiments of references [1–5]. For open dots, where a current can be measured between leads connected to each dot, the problem has been well studied both experimentally and theoretically [6–8]. More recently however, experimental results have been obtained for an isolated double dot system in a GaAs heterostructure [3]. Transfer was forced by varying the gate voltages on one of the dots, and charge transfer detected by a non-invasive voltage probe. Since this system has obvious interest as a possible experimental realization of a q-bit and or as a half cell of a Quantum Cellular Automaton, a good understanding of all mechanisms leading to charge transfer is desirable.

The simplest mechanism for transfer is direct tunneling, also called elastic tunneling; for a critical arrangement of the gate voltages some electron level has a wavefunction equally spread over the two dots, and slight changes in the applied voltage suffice to confine the wavefunction to one or the other of the two. For this to occur it appears necessary to have a doublet of electron states degenerate in energy at the critical configuration. However, initial experimental studies already showed the importance of inelastic tunneling, mediated by acoustic phonons, when the energy separation between the doublet states is approaching the minimum [1]. Although the present generation of experiments has been carried out on two dimensional electron gases (2DEG) defined in very thick heterostructures, similar experiments may be done in future [9] on 2DEG defined in heterostructures consisting of much thinner slabs. It is of interest to examine the effect that changes in the spectrum of phonon modes, due to finite slab thickness, would have on the phonon-assisted tunneling rates. A study along these lines has recently appeared for open double dots [7]. The purpose of the present work is complementary:

we will address the problem of a strongly isolated double dot system using a more realistic model for the confining potential.

II. TWO COUPLED DOTS: SEPARABLE MODEL

In an earlier study [10] on a device similar to that in the experiment of Gardelis *et al* [3], we found that to good approximation a strongly isolated dot was well described by a confining potential of roughly rectangular shape and constant depth surrounded by very steep barriers. To account for leakage of electrons through one side of the dot it was sufficient to use a barrier of finite height and width derived from Poisson Thomas-Fermi simulations. Guided by the success of that model in explaining the lifetimes of the emitted electrons, we will use here a similar confining potential. For simplicity and to achieve satisfactory numerical accuracy, we have chosen a rectangular shape for the barrier separating the two dots. Therefore, in the plane of the 2DEG we consider a double dot of rectangular shape, and define our x and y axes along the directions of its sides. We further set the confining potential, $V(x, y)$, to be infinite outside the boundaries of the rectangle and inside to depend only on x : the profile $V(x)$ is shown in Fig. 1. Dot A on the left has sides $w_l \times l_y$, and dot B on the right, $w_r \times l_y$. The square barrier separating them runs from $-w_b/2$ to $w_b/2$. For convenience we set the zero of energy at the top of the barrier, so that inside dots A and B the potential is $V_D < 0$. The electron wavefunctions, in the envelope function approximation, $\Psi(x, y, z) = \phi(x)\psi(y)\chi(z)$, are obtained by solving a 3D separable Schrödinger equation.

For simplicity, we chose the well known Fang-Howard [12] parametrization for $\chi(z)$, with parameters appropriate for the Cavendish experiment. We give its explicit form in Section III. Due to the simple form of the confining potential along y , the $\psi(y)$ are the well known eigenfunctions of the infinite square well. Along the x axis:

$$-\frac{\hbar^2}{2m^*}\phi''(x) + V(x)\phi(x) = E^{(x)}\phi(x) \quad (1)$$

and $V(x) = V_D$ when $-w_l - w_b/2 < x < -w_b/2$ and $w_b/2 < x < w_b/2 + w_r$, whereas $V(x) = 0$ when $-w_b/2 < x < w_b/2$. The obvious analytic forms of $\phi(x)$ in the “zones” (A, B or barrier) are matched at the boundaries (wavefunction and derivative) leading to explicit equations for the energy that are easily solved numerically to the required accuracy, even for sizeable barriers like those studied here. Once these eigenenergies have been determined it is a simple matter to find the fraction of the normalization of the wavefunctions in each dot. The assignment of each solution to a level in dot A or B is in most cases unambiguously determined by the fractions of normalization. By counting the number of nodes in the corresponding dot we assign to each solution an effective quantum number n_l (left) or n_r (right.) The level crossings which occur for special values of the parameters are detected by the jumps, from almost zero to almost one, of those normalization fractions. There is always negligible normalization inside the barrier.

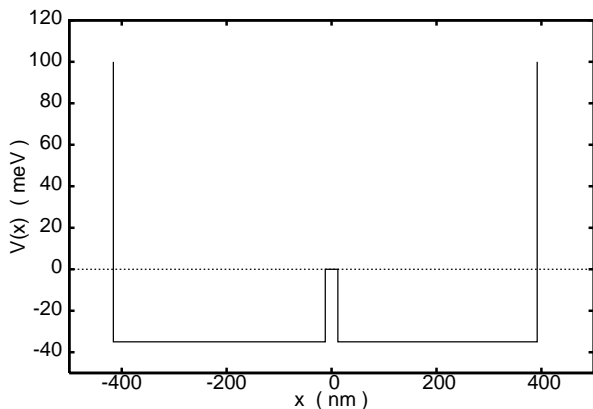


FIG. 1. Confining potential profile along the x direction.

The energy of a given level is the sum of the eigenvalues corresponding to the three eigenfunctions into which $\Psi(x, y, z)$ is factorized. However, in a doublet, the difference of energy between initial and final states has equal contributions from the y and z components since they must have the same $\psi(y)$ and $\chi(z)$. Therefore in what follows $E_{if} = E_{Final}^{(x)} - E_{initial}^{(x)}$.

For definiteness, in the present study we will use the width of dot B, w_r , as the parameter whose variation simulates the changes induced by the variation of one of the confining gate voltages. In Fig. 2 we show the level crossing chosen to present the results of our studies. The parameters for the double dot configuration are: $V_D = -35$ meV, $w_l = 404$ nm, $l_y = 350$ nm, $w_b = 24$ nm and w_r is varied around 380 nm. These parameter values are similar to those used in previous simulations of double

dot devices also measured at the Cavendish [10,11]. The doublet shown corresponds to $n_l = 17$, $n_r = 16$ and with $\psi(y) = \sqrt{2/l_y} \cos(\pi y/l_y)$, has a total energy close to the estimated Fermi level in the double dot system. The continuous lines in the figure are the doublet levels, whereas the dashed lines are inserted to guide the eye and would correspond to the “unperturbed values” of an ideal uncoupled double dot system.

In a simple two-level system described by a hamiltonian:

$$H_{2l} = \begin{pmatrix} E_A & t \\ t & E_B \end{pmatrix}, \quad (2)$$

$\Delta E = \sqrt{(E_A - E_B)^2 + 4t^2}$ is the separation of the two eigenstates. When the two unperturbed values cross, $E_A = E_B$, and $t = \Delta E/2$. This allows one to determine an effective tunneling width which characterizes the coupling between the two dots. From the data shown in Fig. 2 we find $t = 2.2 \mu\text{eV}$.

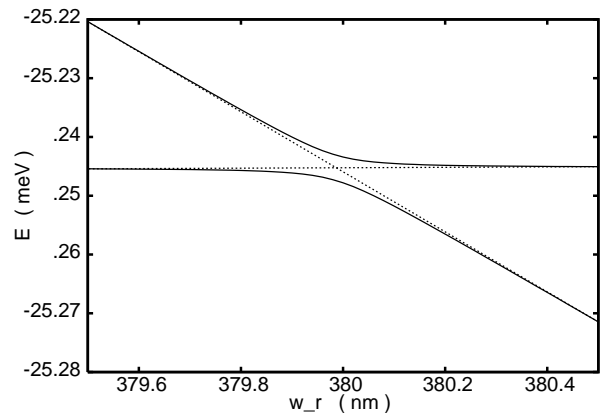


FIG. 2. Energies. Doublet avoided level crossing, $n_r = 16$, $n_l = 17$.

To simulate an experiment we will assume for instance that the initial conditions correspond to $w_r = 380.4$ nm and that the lowest level in the right part of figure 2 (corresponding to dot B) is occupied by one electron and the upper level in the same right part of the figure (dot A) is empty. We then reduce the value of w_r , shrinking the size of dot B but leaving dot A unchanged. The energy of the lowest level increases linearly as w_r decreases so long as the occupation of the corresponding wavefunction stays close to unity in dot A, and stabilizes when the electron tunnels to dot B at about $w_r = 380$ nm. This is direct or elastic tunneling. Inelastic tunneling due to phonon absorption will take place when w_r is still above 380 nm, via transitions from the lower level (electron in dot B) to the upper level (electron in dot A.) In our model we are not dealing explicitly with the coulomb energies of the electron in each well. For the configurations where

the rates are maximal the initial and final electron wavefunctions are equally spread over the two dots, so we can assume that the contribution of Coulomb energy to the doublet separation cancels.

III. ACOUSTIC PHONON RATES FOR A FINITE SLAB HETEROSTRUCTURE

According to Fermi's golden rule, the rate for phonon assisted tunneling is:

$$w = \frac{2\pi}{\hbar} |\langle \Phi_F \Psi_F | H_{e-ph} | \Phi \Psi \rangle|^2 \delta(E - E_F \mp \hbar\omega) \quad (3)$$

where the bras and kets indicate initial and final states of the electron ($|\Psi\rangle$) plus phonons ($|\Phi\rangle$) and the \mp sign applies to phonon emission or absorption. Since GaAs is piezoelectric we will consider both the deformation potential and the piezoelectric contributions to the electron-phonon Hamiltonian. The specific forms of these rates for a finite slab have been thoroughly discussed in the work of Bannov *et al.* [13] which we follow closely. The hamiltonians describing both contributions can be written in second quantized form:

$$H_{e-ph}^{(d,p)} = \sum_{\vec{q}_{\parallel}, n} e^{i\vec{q}_{\parallel} \cdot \vec{r}_{\parallel}} \Gamma_{d/f/s}^{(d,p)}(\vec{q}_{\parallel}, n, z) (c_n(\vec{q}_{\parallel}) + c_n^{\dagger}(-\vec{q}_{\parallel})) \quad (4)$$

with the superscripts d and p indicating deformation and piezoelectric contributions and the subscripts d , f and s dilatational, flexural and shear modes. The z -axis is perpendicular to the plane of the 2DEG and the faces of the slab, and the origin is in the middle of the slab. Vectors in the x, y plane are indicated by the subindex \parallel , and n is the mode index. The expressions for the various Γ 's are found in equations 33-34 (deformation potential) and 39-41 (piezoelectric) of [13]. Particularizing to the separable electron wavefunctions of our model:

$$w^{(d,p)} = \frac{2\pi}{\hbar} \sum_{\vec{q}_{\parallel}, n} \mathcal{M}_{\parallel} |\langle \chi(z) | \Gamma_{d/f/s}^{(d,p)}(\vec{q}_{\pm}, n, z) | \chi(z) \rangle|^2 \times \left(N(\hbar\omega_n) + \frac{1}{2} \pm \frac{1}{2} \right) \delta(E - E' \mp \hbar\omega_n), \quad (5)$$

where we have evaluated the matrix elements corresponding to the phonon occupations, and defined

$$\mathcal{M}_{\parallel} \equiv |\langle \phi_F(x)\psi(y) | e^{i\vec{q}_{\parallel} \cdot \vec{r}_{\parallel}} | \phi(x)\psi(y) \rangle|^2. \quad (6)$$

We remark that Bannov *et al.* [13] chose the axes in the 2DEG plane so that $\vec{q}_{\parallel} = (q_x, 0)$, whereas we have aligned the x and y directions along the sides of the double dot. Therefore, the q_x appearing in their work correspond to $|\vec{q}_{\parallel}| \equiv q_{\parallel}$ in ours. Accordingly, we write:

$$\mathcal{M}_{\parallel} = |\langle \phi_F(x) | e^{iq_{\parallel} x \cos \theta_{\parallel}} | \phi(x) \rangle|^2 \times |\langle \psi(y) | e^{iq_{\parallel} y \sin \theta_{\parallel}} | \psi(y) \rangle|^2. \quad (7)$$

To show the coupling constants explicitly, we rewrite the Γ 's as follows:

$$\Gamma_{d/f}^{(d)}(\vec{q}_{\parallel}, n, z) \equiv F_{d/f,n} \sqrt{\frac{\hbar E_a^2}{2A\rho \omega(\vec{q}_{\parallel})}} \gamma_{d/f,n}^{(d)}(q_{\parallel}, q_t, q_t; z)$$

$$\Gamma_{d/f/s}^{(p)}(\vec{q}_{\parallel}, n, z) \equiv F_{d/f/s,n} \frac{8\pi e\beta}{\epsilon} \sqrt{\frac{\hbar}{2A\rho \omega_n(\vec{q}_{\parallel})}} \times \gamma_{d/f/s,n}^{(p)}(q_{\parallel}, q_t, q_t; z), \quad (8)$$

with explicit expressions for the γ 's to be found in the above mentioned equations of [13]. The normalization factors, $F_{d/f/s}$ are given in their appendix. In this revised notation, the deformation rate becomes

$$w^{(d)} = \frac{1}{2\pi\hbar} \sum_{n;d,f} \int d\vec{q}_{\parallel} \mathcal{M}_{\parallel} F_n^2 \frac{\hbar E_a^2}{2\rho\omega_n(\vec{q}_{\parallel})} \times |\langle \chi(z) | \gamma_n^{(d)}(z) | \chi(z) \rangle|^2 \times \left(N(\hbar\omega_n) + \frac{1}{2} \mp \frac{1}{2} \right) \delta(E - E_F \mp \hbar\omega_n), \quad (9)$$

where we have omitted the subindexes d/f that appear each time a mode n is referenced. A similar expression applies to the piezoelectric rates. Furthermore, for an infinite slab area, one has to replace $1/A \sum_{\vec{q}_{\parallel}}$ by the integral $(1/(2\pi)^2) \int d\vec{q}_{\parallel} = (1/(2\pi)^2) \int q_{\parallel} dq_{\parallel} d\theta_{\parallel}$, so that

$$\int_0^{2\pi} d\theta_{\parallel} \int_0^{\infty} q_{\parallel} dq_{\parallel} \delta(E - E_F - \hbar\omega) = \int_0^{2\pi} d\theta_{\parallel} q_{\parallel} \left(\frac{d\hbar\omega}{dq_{\parallel}} \right)^{-1}. \quad (10)$$

We then arrive at

$$w^{(d)} = \frac{\hbar}{4\pi} \sum_{n;d,f,s} \frac{E_a^2 q_{\parallel}}{\rho \hbar\omega_n (d\hbar\omega_n/dq_{\parallel})} \left(N\hbar\omega_n + \frac{1}{2} \mp \frac{1}{2} \right) \times F_n^2 |\langle \chi(z) | \gamma_n^{(d)}(z) | \chi(z) \rangle|^2 \bar{\mathcal{M}}_{\parallel}, \quad (11)$$

where

$$\bar{\mathcal{M}}_{\parallel} \equiv \int_0^{2\pi} d\theta_{\parallel} \mathcal{M}_{\parallel}. \quad (12)$$

To determine the expectation values of the γ 's we have chosen a Fang-Howard wavefunction to represent $\chi(z)$:

$$\chi(z) = \frac{1}{\sqrt{2}} b^{3/2} (z - \bar{z}_0) e^{-b(z - \bar{z}_0)/2}, \quad z > \bar{z}_0$$

$$= 0, \quad z < \bar{z}_0. \quad (13)$$

with $\bar{z} = a/2 - z$ and \bar{z}_0 is the depth of the 2DEG referred to the surface of the slab. We have chosen $\bar{z}_0 = 70$ nm and $b = 1/4$ nm⁻¹.

We solved the algebraic equations (13),(14) and (18) of [13] numerically, so as to obtain the dispersion relation $\hbar\omega_n(q_{\parallel})$ and corresponding expressions for the other momenta q_t and q_l appearing in the explicit expressions for the $\gamma_n^{(d,p)}(z)$ and the normalization factors F_n^2 .

IV. RESULTS

Before presenting results for the rates, it is interesting to discuss some general features of the terms appearing in eq. 11 and their dependence on the doublet energy splitting, E_{if} . For a given mode, the corresponding dispersion relation $E_{if} = \hbar\omega_n(q_{\parallel}; a)$ determines the momenta q_{\parallel} , q_t and q_l . As shown in figure 2, to a good approximation one finds the same value of the splitting energy for pairs of points located symmetrically with respect to the crossing point at $w_{r,cross} \simeq 380$ nm. One such pair is $w_{r,1} = 379.8$ nm, $w_{r,2} = 380.2$ nm. For these two the values of q_{\parallel} are nearly the same. This implies that all factors contributing to eq. 11 except $\bar{\mathcal{M}}_{\parallel}$ will also be almost equal since they depend only on q_{\parallel} . The matrix element $\bar{\mathcal{M}}_{\parallel}$ involves the doublet wavefunctions $\phi(x)$ and $\phi_F(x)$ and these depend on the value of w_r . It turns out however that due to the simplicity of the potential profile chosen for $V(x)$, the products of wavefunctions for the paired doublets are also very similar. This is shown in Fig. 3, where we have plotted the overlaps $\phi_F(x)\phi(x)$ for the doublets $w_{r,1} = 379.8$ nm (continuous line) and $w_{r,2} = 380.2$ nm (dashed line). For clarity of the figure we only show the range $-100 < x < 100$ nm, but the two lines practically coincide in most of the range of x 's. If we had chosen $w_{r,1} = 379.77$ nm, so as to make the two E_{if} even closer, the two lines in the plot would be indistinguishable

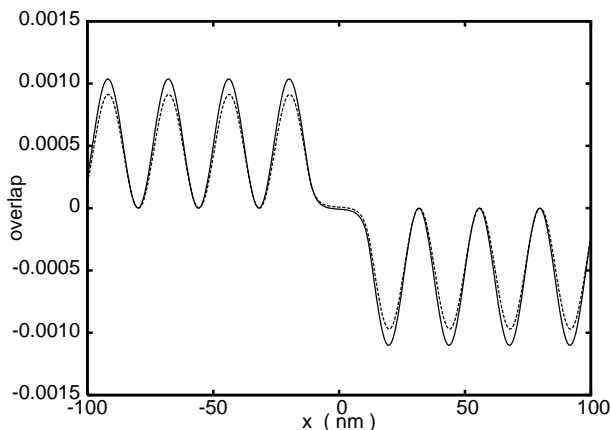


FIG. 3. Overlaps of wavefunctions. Continuous line: the $\phi_F(x)\phi(x)$ of the pair corresponding to $w_r = 379.8$ nm. Dashed line: same for the pair at $w_r = 380.2$ nm.

The result of this symmetry is that the matrix element $\bar{\mathcal{M}}_{\parallel}$ is nearly identical for the two cases, since it is determined by the overlaps. In summary: the rates are very similar for pairs with w_r symmetric with respect to the crossing point. Part of this is due to the simplicity of the potential profile chosen, but as long as the potential profile at the barrier is symmetric and each dot has a wide flat potential well, we expect that this symmetry will be

preserved by less schematic double dot potential profiles.

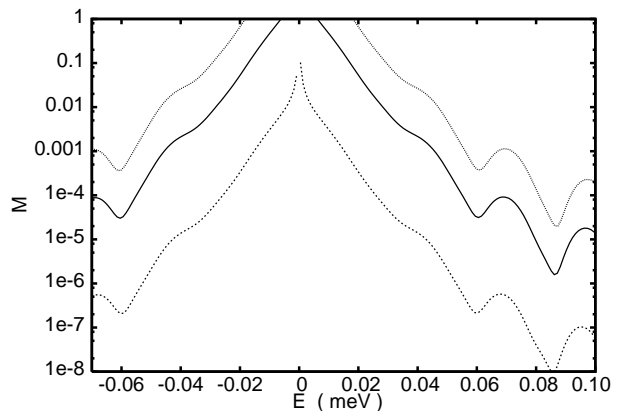


FIG. 4. Matrix element $\bar{\mathcal{M}}_{\parallel}$ for various barrier widths: Continuous line $w_b = 24$ nm ($t_{eff} = 2.2\mu\text{eV}$), dotted line: $w_b = 18$ nm ($t_{eff} = 7.6\mu\text{eV}$), dashed line: $w_b = 36$ nm ($t_{eff} = 0.2\mu\text{eV}$).

Fig.4 shows $\bar{\mathcal{M}}_{\parallel}$ for three barrier widths. One sees that indeed the curves are symmetric with respect to $E_{if} = 0$, and that the magnitude depends strongly on w_b . However, their shape depends little on the barrier width, showing the expected increase at small doublet energies. To analyze the latter, it is useful to consider the contributions to $\bar{\mathcal{M}}_{\parallel}$ for very low q_{\parallel} . When $q_{\parallel} \rightarrow 0$, eq. 7 can be approximated by

$$\mathcal{M}_{\parallel} \simeq q_{\parallel}^2 \cos^2 \theta_{\parallel} | \langle \phi_F(x) | x | \phi(x) \rangle |^2 . \quad (14)$$

Fig. 5 shows these matrix elements \mathcal{M} for a configuration with $w_r = 379.9$ nm and $\psi(y)$ the lowest energy solution for the infinite square well. It can be seen that $q_{\parallel} \simeq 4.5 \cdot 10^{-3} \text{ nm}^{-1}$ (corresponding to $E_{if} \simeq 6.1\mu\text{eV}$) is not sufficiently close to 0 and therefore eq. 14 gives only a rough approximation for most values of θ_{\parallel} . For other values of w_r the agreement is similar. Eq. 14 is nevertheless useful because it correlates \mathcal{M}_{\parallel} with the expectation value of x , and the behaviour of the latter is easier to visualize:

For large doublet splitting the overlap of the wavefunctions $\phi(x)$ and $\phi_F(x)$ is small: one is mainly located in dot A, the other in B. As E_{if} decreases each wavefunction begins to spread into the other dot. At the minimal doublet splitting, and assuming for sake of argument equal dot sizes, the wavefunctions become a symmetric and antisymmetric pair each with equal occupations in the two dots. The overlap is then maximal, but the product $\phi(x)\phi_F(x)$ is of positive sign in one dot and negative in the other so the resulting overlap integral vanishes. Introducing an x in the integration, as in eq. 14, makes the contributions from the two dots equal and therefore maximizes the matrix element when the two eigenfunctions are maximally spread over the two dots.

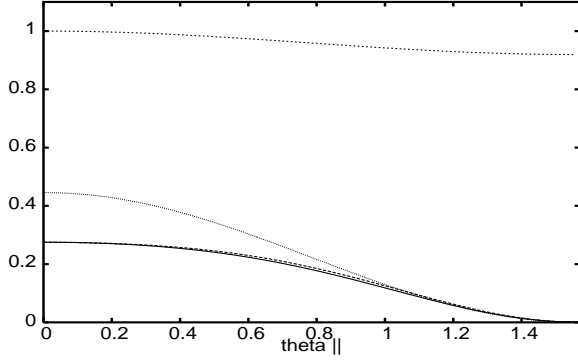


FIG. 5. The matrix elements entering \mathcal{M} v.s. θ_{\parallel} ; two dot system with $w_r = 379.9$ nm. Continuous line: Full \mathcal{M} . Close by dashed line: $|\langle \phi_F | e^{iq_{\parallel} \cos \theta_{\parallel}} | \phi \rangle|^2$. Short dashed line at top: $|\langle \psi_F | e^{iq_{\parallel} \sin \theta_{\parallel}} | \psi \rangle|^2$. Dotted line: approximate \mathcal{M} of eq. 14.

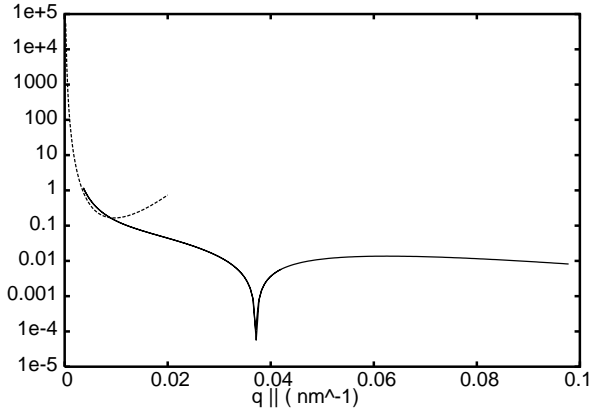


FIG. 6. Matrix element \mathcal{N} as a function of q_{\parallel} for the lowest flexural mode. Continuous line: exact numerical calculation. Dashed line: small q_{\parallel} expansion.

To complete the analysis, we show in Fig. 6 the matrix element: $\mathcal{N} \equiv |F_f \langle \chi(z) | \gamma_n^{(p)}(z) | \chi(z) \rangle|^2$, for the lowest flexural mode. As will be shown in next section this mode gives the dominant contribution to the rate at small doublet splittings. At very small q_{\parallel} one can perform power series expansions of the quantities entering into this matrix element and, neglecting the 2DEG thickness, one finds

$$\mathcal{N} \simeq \frac{18s_l^2}{a^{9/2}s_t^2} \frac{\cosh(q_{\parallel}a/2) \cosh(q_{\parallel}(a/2 - \bar{z}_0))}{(1 - (s_t/s_l)^2)^2 q_{\parallel}^4}, \quad (15)$$

where s_l and s_t are the velocities of bulk longitudinal and transverse waves. This approximation is shown as a

dashed line in Fig. 6 and reveals the cause of the sharp increase when $q_{\parallel} \rightarrow 0$. In conclusion, the two matrix elements, \mathcal{M}_{\parallel} and \mathcal{N} contribute to the strong increase of the piezoelectric rates at small doublet energies, to be shown next.

Rates: Following ref. [3], we have chosen $T = 100$ mK for all our rate calculations. Also, for definiteness, we have assumed that one of the symmetry axes of GaAs is parallel to z , whereas the other two are in the plane of the 2DEG, rotated by an angle $\theta_{sym} = \pi/5$ with respect to the x, y axes introduced above. The material parameters and coupling constants for GaAs were taken from [14,15]. As discussed at the beginning of this section, to the accuracy of the logarithmic graphs to be presented, the rates for pairs of states with the same energy difference E_{if} are indistinguishable. To present emission and absorption rates in the same graph, we adopt the convention that negative (positive) E_{if} correspond to phonon absorption (emission). Again, to the accuracy of the graphs, the difference between the two rates for the same $|E_{if}|$ is entirely due to the factor $N(E_{if}) + 1/2 \pm 1/2$.

In Figs. 7 to 9 we present the rates for a slab of thickness $a = 500$ nm, for the doublet shown in Fig. 2. The 2DEG is located at a depth $\bar{z}_0 = 70$ nm below the surface and $\psi(y)$ is the lowest eigenfunction of the square well. Note the different scales in Fig. 7 from the rest. This reflects the dominant role of piezoelectric rates due to flexural modes, particularly at small doublet energies. In Fig. 7, we show the piezoelectric rates due to the flexural modes. The various dashed and dotted lines show the separate contributions for each mode, and the continuous line is the sum of all. Note that only the lowest flexural mode has a dispersion relation such that $\hbar\omega \rightarrow 0$ when $q_{\parallel} \rightarrow 0$ so that it contributes to all doublet separations. Higher modes tend to a finite energy when $q_{\parallel} \rightarrow 0$ and therefore their contributions start at increasing non-zero threshold values of E_{if} . Note that at small $|E_{if}|$ the long dashed line corresponding to the lowest flexural mode is indistinguishable from the sum due to the negligible contribution of the remaining modes.

At the beginning of this section we have already explained the strong increase in this rate when $E_{if} \rightarrow 0$. As the doublet separation increases the total rate decreases, with oscillations that only appear smooth due to use of a logarithmic plot, but which have significant features: at around $30 \mu\text{eV}$ one sees a sharp jump due to the threshold of the third flexural mode and a pronounced dip is seen at $60 \mu\text{eV}$ due to the oscillating contribution of the fifth mode. For the same flexural modes, the rates at small doublet energies are roughly eight orders of magnitude larger than those of the deformation potential interaction. Only at the threshold ~ 0.1 meV does the deformation rate reach a value comparable to the piezoelectric rate. The deformation rates might perhaps be more relevant in dots defined on a less piezoelectric semiconductor, such as InAs.

Figs. 8 and 9 show the piezoelectric rates due to shear

and dilatational modes. They are of similar magnitude to each other, and only beyond $50 \mu\text{eV}$ do they become comparable to the flexural ones. Note also that they become very small at the lowest doublet separations. The deformation rates due to the dilatational modes are always one to two orders of magnitude smaller than the corresponding piezoelectric rates.

The dependence of the rates on slab thickness is shown in Figs. 10 to 12. In Fig. 10 we show piezoelectric rates due to flexural modes, for a fixed doublet splitting energy that corresponds to $w_r = 379.9 \text{ nm}$ ($E_{if} \simeq 6.1 \mu\text{eV}$.) The contribution from the lowest flexural mode (continuous line) dominates the others (dashed and dotted lines) over the whole range of thicknesses considered. Interestingly, increasing a from 500 to 2000 nm reduces the total rate by two orders of magnitude, showing the importance of finite slab thickness in determining rates.

Fig. 11 examines the dependence of that reduction on the 2DEG depth. Bringing \bar{z}_0 closer to the surface increases the rates further, by about 25% in going from a depth of 70 nm to 35 nm. Finally, Fig. 12 shows the difference in rates between a “surface” and a “bulk” 2DEG: the location of the 2DEG has been set at $\bar{z}_0 = a/2 - 180 \text{ nm}$ and a has been varied. The configuration, $a = 500 \text{ nm}$, which sets $\bar{z}_0 = 70 \text{ nm}$, was our standard configuration in all previous graphs. Now, as a is increased, the 2DEG stays near the center of the slab, and its distance to the surface increases. One can see in Fig. 12 two distinct regimes: “surface”: for small slab thicknesses the total rate due to all flexural modes decreases exponentially by as much as five orders of magnitude; ii) “bulk” beyond $a \simeq 2000 \text{ nm}$ the rate stabilizes in order of magnitude, but oscillations of up to a factor of 2 still persist. The contributions to the rate due to shear and dilatational modes (not shown) are totally negligible at small a and show a similar stabilization for a above 2000 nm, where they are still one order of magnitude smaller than the flexural ones. Although experiments with a 2DEG at such depths are unrealistic, these results highlight the danger of estimating the rates for a double dot system without considering the influence of surface boundary conditions on the phonon spectrum.

V. CONCLUSIONS

We have studied the main features of the tunneling rates between a doublet of states in a well-isolated two dot system defined on a slab of finite thickness. At low temperatures, $T = 100 \text{ mK}$, and for a piezoelectric material (GaAs), our results confirm the dominance of the piezoelectric over the deformation rates. At small doublet separations we find that the lowest piezoelectric flexural mode gives the dominant contribution. Keeping the 2DEG at a fixed depth from the surface and increasing the slab thickness we find that the rates vary as much as two orders of magnitude, increasing as the slab thickness

is decreased. Therefore in thin slabs the effective electron to acoustic phonon coupling is greatly enhanced. Complementarily, as a way to stress the relevance of boundary conditions on the phonon spectrum, when we keep the 2DEG near the middle of the slab and increase its thickness, we find that the “bulk” configuration leads to substantially smaller rates than the “surface” one. These findings should be useful in the design of future experiments on double dot systems supported on finite slabs.

ACKNOWLEDGMENTS

Useful discussions with C.G. Smith are gratefully acknowledged. We are grateful to NSERC Canada for Discovery Grant RGPIN-3198 (DWLS) and to DGES-Spain for continued support through grants BFM2001-3710 and FIS2004-03156 (JM). Guo Hong Yun is a visiting scholar at McMaster on research leave from IMU.

-
- ¹ T. Fujisawa, T.H. Oosterkamp, W.G. van der Wiel, B. W. Broer, R. Aguado, S. Tarucha and L.P. Kouwenhoven, *Science* **282** (1998) 932-5.
 - ² H. Qin, A.W. Holleitner, K. Ebert and R.H. Blick, *Phys. Rev. B* **64** (2002) 241302 and cond-mat/0011155.
 - ³ S. Gardelis, C.G. Smith, J. Cooper, D.A. Richtie, E.H. Linfield, Y. Jin and M. Pepper, *Phys. Rev. B* **67** (2003) 073302.
 - ⁴ T. Hayashi, T. Fujisawa, H.D. Cheng, Y.H. Jeong and Y. Hirayama, *Phys. Rev. Letters* **91** (2003) 226804.
 - ⁵ L. DiCarlo, H.J. Lynch, A.C. Johnson, L.I. Childress, K. Crockett, C.M. Marcus, M.P. Hanson and A.C. Gossard, *Phys. Rev. Letters* **92** (2004) 226801.
 - ⁶ T. Brandes and B. Kramer, *Phys. Rev. Letters* **83** (1999) 3021-3024.
 - ⁷ S. Debal, T. Brandes and B. Kramer, *Phys. Rev. B* **66** (2002) 041301.
 - ⁸ T. Brandes, R. Aguado and G. Platero, *Phys. Rev. B* **69** (2004) 205326.
 - ⁹ C.G. Smith, private communication.
 - ¹⁰ J. Martorell, D.W.L. Sprung, P. Machado and C.G. Smith, *Phys. Rev. B* **63** (2001) 181572.
 - ¹¹ See progress reports of the Esprit project QUADRANT (Quantum Devices for Advanced Nanoelectronic Technology), available at <http://quadrant.iet.unipi.it>.
 - ¹² F.F. Fang and W.E. Howard, *Phys. Rev. Lett.* **16** (1966) 797.
 - ¹³ N. Bannov, V. Mitin and M. Stroschio, *Phys. Stat. Sol.(b)* **183** (1994) 131.
 - ¹⁴ B.A. Glavin, V.I. Pipa, V.V. Mitin and M. A. Stroschio, *Phys. Rev. B* **65** (2002) 205315.
 - ¹⁵ V.V. Mitin, V.A. Kochelap, M.A. Stroschio, “Quantum Heterostructures”, Cambridge U. Press, (1999), ISBN 0 521 63635 3.

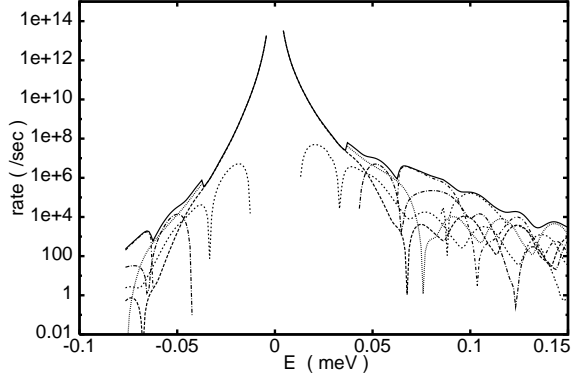


FIG. 7. Piezoelectric rates due to flexural modes, as a function of doublet splitting. Continuous line sum of all contributions. Dashed lines : separate contributions of each of the modes

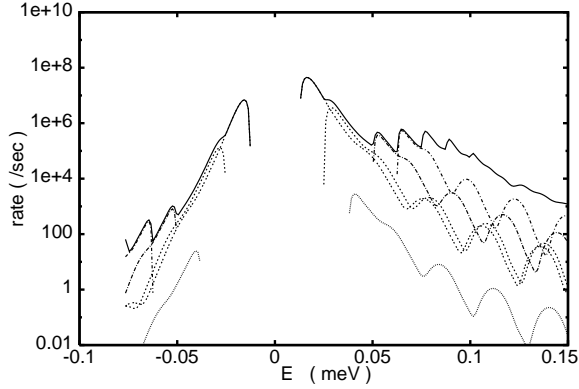


FIG. 8. Piezoelectric rates due to shear modes, as a function of doublet splitting.

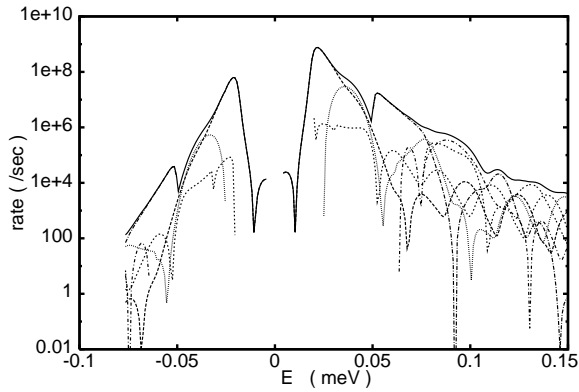


FIG. 9. Piezoelectric rates due to dilatational modes, as a function of doublet splitting.

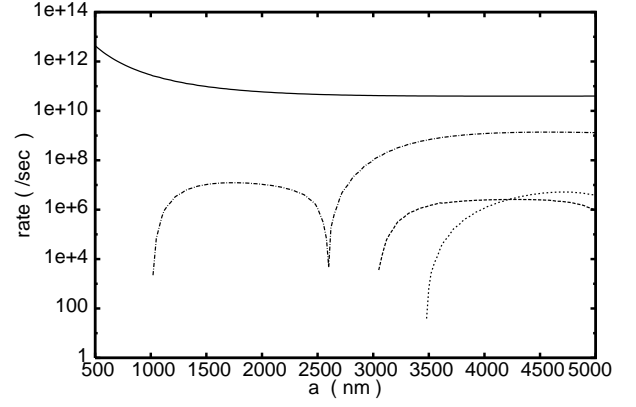


FIG. 10. Piezoelectric rates due to flexural modes, for fixed $w_r = 379.9$ nm ($E_{if} = 6.1\mu\text{eV}$), as a function of slab thickness a . Continuous line: contribution of the lowest mode. Dashed lines : other modes.

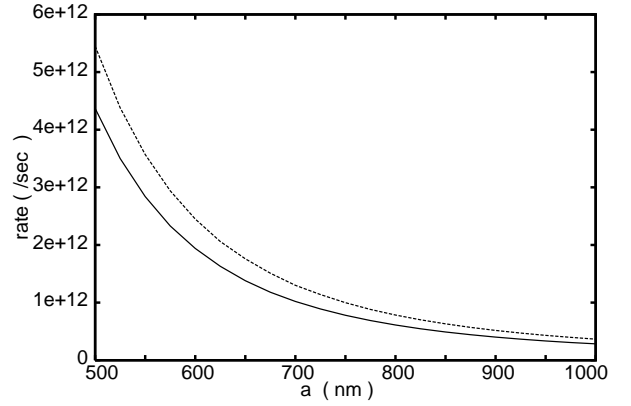


FIG. 11. Piezoelectric rates for the lowest flexural mode, for fixed $w_r = 379.9$ nm ($E_{if} = 6.1\mu\text{eV}$), as a function of slab thickness a ; $\bar{z}_0 = 70$ nm (continuous line), $\bar{z}_0 = 35$ nm (dashed) .

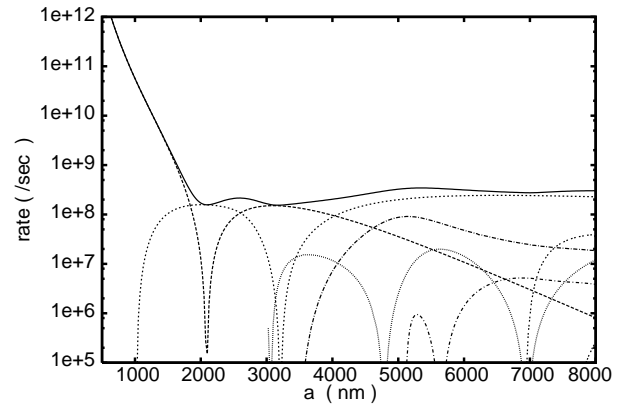


FIG. 12. Piezoelectric rates due to the flexural modes, for $w_r = 379.9$ nm ($E_{if} = 6.1\mu\text{eV}$) and $\bar{z}_0 = a/2 - 180$ nm, against a . Dashed lines: individual modes; continuous line, total.